Properties of starless and prestellar cores in Taurus revealed by *Herschel*[*] SPIRE/PACS imaging

K. A. Marsh,[1]† M. J. Griffin,[1] P. Palmeirim,[2] Ph. André,[2] J. Kirk,[3] D. Stamatellos,[3] D. Ward-Thompson,[3] A. Roy,[2] S. Bontemps,[4,5] J. Di Francesco,[6] D. Elia,[7] T. Hill,[8] V. Könyves,[2,9] F. Motte,[2] Q. Nguyen-Luong,[10] N. Peretto,[1] S. Pezzuto,[7] A. Rivera-Ingraham,[11,12] N. Schneider,[4,5] L. Spinoglio[7] and G. White[13,14]

[1]*School of Physics and Astronomy, Cardiff University, Cardiff CF24 3AA, UK*
[2]*Laboratoire AIM, CEA/DSM-CNRS-Université Paris Diderot, IRFU/Service d'Astrophysique, C.E. Saclay, Orme des Merisiers, F-91191 Gif-sur-Yvette, France*
[3]*Jeremiah Horrocks Institute for Astrophysics and Supercomputing, University of Central Lancashire, Preston PR1 2HE, UK*
[4]*Univ. Bordeaux, LAB, UMR 5804, F-33270 Floirac, France*
[5]*CNRS, LAB, UMR 5804, F-33270 Floirac, France*
[6]*Hertzberg Institute of Astrophysics, National Research Council of Canada, 5071 West Saanich Rd., Victoria, BC V9E 2E7, Canada*
[7]*Istituto di Astrofisica e Planetologia Spaziali – INAF, Via Fosso del Cavaliere 100, I-00133 Roma, Italy*
[8]*Joint ALMA Observatory, Alonso de Cordova 3107, Vitacura 763-0355, Santiago, Chile*
[9]*Institut d'Astrophysique Spatiale, UMR8617, CNRS/Université Paris-Sud 11, F-91405 Orsay, France*
[10]*Department of Astronomy & Astrophysics, University of Toronto, 50 George Street, Toronto, ON M5S 3H4, Canada*
[11]*Université de Toulouse, UPS-OMP, IRAP, Toulouse, France*
[12]*CNRS, IRAP, 9 Av. Colonel Roche, BP 44346, F-31028 Toulouse Cedex 4, France*
[13]*Department of Physics and Astronomy, The Open University, Walton Hall, Milton Keynes, MK7 6AA, UK*
[14]*RALSpace, Rutherford Appleton Laboratory, Chilton, Didcot OX11 0NL, UK*

ABSTRACT

The density and temperature structures of dense cores in the L1495 cloud of the Taurus star-forming region are investigated using *Herschel* Spectral and Photometric Imaging Receiver and Photodetector Array Camera and Spectrometer images in the 70, 160, 250, 350 and 500 µm continuum bands. A sample consisting of 20 cores, selected using spectral and spatial criteria, is analysed using a new maximum likelihood technique, COREFIT, which takes full account of the instrumental point spread functions. We obtain central dust temperatures, T_0, in the range 6–12 K and find that, in the majority of cases, the radial density falloff at large radial distances is consistent with the asymptotic r^{-2} variation expected for Bonnor–Ebert spheres. Two of our cores exhibit a significantly steeper falloff, however, and since both appear to be gravitationally unstable, such behaviour may have implications for collapse models. We find a strong negative correlation between T_0 and peak column density, as expected if the dust is heated predominantly by the interstellar radiation field. At the temperatures we estimate for the core centres, carbon-bearing molecules freeze out as ice mantles on dust grains, and this behaviour is supported here by the lack of correspondence between our estimated core locations and the previously published positions of $H^{13}CO^+$ peaks. On this basis, our observations suggest a sublimation-zone radius typically $\sim 10^4$ au. Comparison with previously published N_2H^+ data at 8400 au resolution, however, shows no evidence for N_2H^+ depletion at that resolution.

Key words: methods: data analysis – techniques: high angular resolution – stars: formation – stars: protostars – ISM: clouds – submillimetre: ISM.

1 INTRODUCTION

A key step in the star formation process is the production of cold dense cores of molecular gas and dust (Ward-Thompson et al. 1994; André, Ward-Thompson & Motte 1996). Cores which do not

contain a stellar object are referred to as *starless*; an important subset of these consists of *prestellar* cores, i.e. those cores which are gravitationally bound and therefore present the initial conditions for protostellar collapse.

Observations of cold cores are best made in the submillimetre regime in which they produce their peak emission, and observations made with ground-based telescopes have previously helped to establish important links between the stellar initial mass function and the core mass function (CMF; Motte, André & Neri 1998). With the advent of *Herschel* (Pilbratt et al. 2010), however, these cores can now be probed with high-sensitivity multiband imaging in the far-infrared and submillimetre, and hence the CMF can be probed to lower masses than before. One of the major goals of the *Herschel* Gould Belt Survey (HGBS; André et al. 2010) is to characterize the CMF over the densest portions of the Gould Belt. This survey covers 15 nearby molecular clouds which span a wide range of star formation environments; preliminary results for Aquila have been reported by Könyves et al. (2010). Another *Herschel* key programme, HOBYS ('*Herschel* imaging survey of OB Young Stellar objects') (Motte et al. 2010) is aimed at more massive dense cores and the initial conditions for high-mass star formation, and preliminary results have been presented by Giannini et al. (2012).

The Taurus Molecular Cloud is a nearby region of predominantly non-clustered low-mass star formation, at an estimated distance of 140 pc (Elias 1978), in which the stellar density is relatively low and objects can be studied in relative isolation. Its detailed morphology at *Herschel* wavelengths is discussed by Kirk et al. (2013). The region is dominated by two long (∼3°), roughly parallel filamentary structures, the larger of which is the northern structure. Early results from *Herschel* regarding the filamentary properties have been reported by Palmeirim et al. (2013).

In this paper, we focus on the starless core population of the field with particular interest in core structure and star-forming potential. Our analysis is based on observations of the western portion of the northern filamentary structure, designated as N3 in Kirk et al. (2013), which includes the Lynds cloud L1495 and contains Barnard clouds B211 and B213 as prominent subsections of the filament. Our analysis involves a sample of 20 cores which we believe to be representative of relatively isolated cores in this region. The principal aims of the study are as follows:

(i) accurate mass estimation based on models which take account of radial temperature variations and which use spatial and spectral data;

(ii) a comparison of these results with those from simpler techniques commonly used for estimating the CMF in order to provide a calibration benchmark for such techniques;

(iii) investigation of processes such as heating of the dust by the interstellar radiation field (ISRF) and the effect of temperature gradients on core stability;

(iv) examination of the results in the context of other observations of the same cores where possible, particularly with regard to gaining insight into the relationship between the dust and gas.

The estimation of the core density and temperature structures is achieved using our newly developed technique, COREFIT, complementary in some ways to the recently used Abel transform method (Roy et al. 2013). Before discussing COREFIT and its results in detail, we first describe our observations and core selection criteria.

2 OBSERVATIONS

The observational data for this study consist of a set of images of the L1495 cloud in the Taurus star-forming region, made on 2010 February 12 and 2010 August 7–8, during the course of the HGBS. The data were taken using Photodetector Array Camera and Spectrometer (PACS; Poglitsch et al. 2010) at 70 and 160 μm and Spectral and Photometric Imaging Receiver (SPIRE; Griffin et al. 2010) at 250, 350 and 500 μm in fast scanning (60 arcsec s^{-1}) parallel mode. The *Herschel* Observation IDs were 1342202254, 1342190616 and 1342202090. An additional PACS observation (ID 1342242047) was taken on 2012 March 20 to fill a data gap. Calibrated scan-map images were produced in the HIPE Version 8.1 pipeline (Ott 2010) using the Scanamorphos (Roussel 2013) and 'naive' map-making procedures for PACS and SPIRE, respectively. A detailed description of the observational and data reduction procedures is given in Kirk et al. (2013).

3 CANDIDATE CORE SELECTION

The first step in our core selection procedure consists of source extraction via the *getsources* algorithm[1] (Men'shchikov et al. 2012) which uses the images at all available wavelengths simultaneously. These consist of the images at all five *Herschel* bands plus a column density map which is used as if it were a sixth band, the purpose being to give extra weight to regions of high column density in the detection process. The column density map itself is obtained from the same set of SPIRE/PACS images, using the procedure described by Palmeirim et al. (2013) which provides a spatial resolution corresponding to that of the 250 μm observations.

The detection list is first filtered to remove unreliable sources. This is based on the value of the 'global goodness' parameter (Men'shchikov et al. 2012) which is a combination of various quality metrics. It incorporates the quadrature sums of both the 'detection significance' and signal-to-noise ratio (S/N) over the set of wavebands, as well as some contrast-based information. The 'detection significance' is defined with respect to a spatially bandpass-filtered image, the characteristic spatial scale of which matches that of the source itself. At a given band, the detection significance is then equal to the ratio of peak source intensity to the standard deviation of background noise in this image. The S/N is defined in a similar way, except that it is based on the observed, rather than filtered, image.

For present purposes, we require a 'global goodness' value greater than or equal to 1. A source satisfying this criterion may be regarded as having an overall confidence level ≥7σ and can therefore be treated as a robust detection. Classification as a core for the purpose of this study then involves the following additional criteria:

(i) detection significance (as defined above) greater than or equal to 5.0 in the column density map;

(ii) detection significance greater than or equal to 5.0 in at least *two* wavebands between 160 and 500 μm;

(iii) detection significance *less than* 5.0 for the 70 μm band and no visible signature on the 70 μm image, in order to exclude protostellar cores, i.e. those cores which contain a protostellar object;

(iv) ellipticity less than 2.0, as measured by *getsources*;

(v) source not spatially coincident with a known galaxy, based on comparison with the NASA Extragalactic Database.

This procedure resulted in a total of 496 cores over the observed 2°.2 × 2°.2 region. The total mass, 88 M$_{\odot}$, of the detected cores represents approximately 4 per cent of the mass of the L1495 cloud, estimated to be 1500–2700 M$_{\odot}$ (Kramer & Winnewisser 1991). From this set, 20 cores were selected for detailed study. The main

---

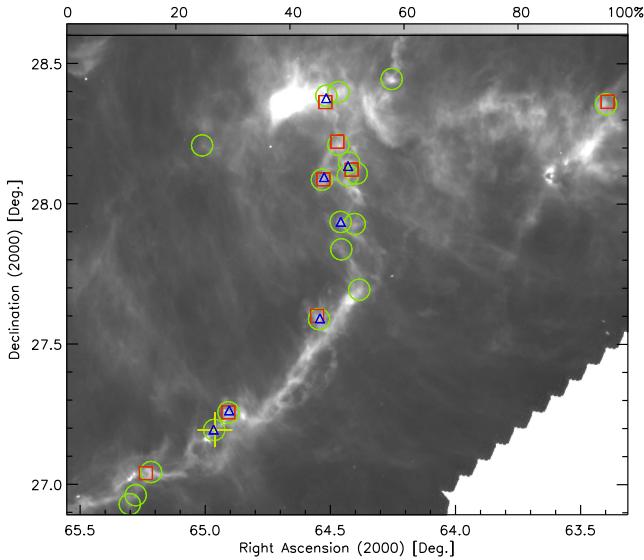[1] Version 1.130401 was used for the analysis described here.

Figure 1. SPIRE 250 μm image of the L1495 region. The green circles represent the locations of the 20 cores selected for modelling. The other symbols represent previously published core locations at other wavelengths; red squares: $H^{13}CO^+$ (Onishi et al. 2002); blue triangles: N_2H^+ (Hacar et al. 2013); yellow cross: 850 μm (Sadavoy et al. 2010). The image is shown on a truncated intensity scale in order to emphasize a faint structure; the display saturates at 200 MJy sr^{-1} which corresponds to 100 per cent on the grey-scale.

goal of the final selection process was to obtain a list of relatively unconfused cores, uniformly sampled in mass according to preliminary estimates obtained via spectral energy distribution (SED) fitting as outlined in the next section. Cores which were multiply peaked or confused, based on visual examination of the 250–500 μm images, were excluded. The mass range 0.02–2.0 M$_\odot$ was then divided into seven bins, each of which spanned a factor of 2 in mass, and a small number of objects (nominally three) selected from each bin. The selection was made on a random basis except for a preference for objects for which previously published data were available, thus facilitating comparison of deduced parameters. Fig. 1 shows the locations of the 20 selected cores on a SPIRE 250 μm image of the field.

4 SED FITTING

Preliminary values of core masses and dust temperatures are estimated by fitting a grey-body spectrum to the observed SED constructed from the set of five wavelength *getsources* fluxes. For this computation, sources are assumed to be isothermal and have a wavelength variation of opacity of the form (Hildebrand 1983; Roy et al. 2013)

$$\kappa(\lambda) = 0.1\,(300/\lambda_{[\mu m]})^2 \qquad cm^2\,g^{-1}. \tag{1}$$

Although obtained observationally, the numerical value of the coefficient in this relation is consistent with a gas-to-dust ratio of 100.

5 CORE PROFILING

To obtain better estimates of core mass and other properties, a more detailed model fit is required. For this purpose, we have developed a new procedure, COREFIT, which involves maximum likelihood estimation using both spatial and spectral information.

The fitting process involves calculating a series of forward models, i.e. sets of model images based on assumed parameter values, which are then compared with the data. The models are based on spherical geometry, in which the radial variations of volume density and temperature are represented by parametrized functional forms. For a given set of parameters, a model image is generated at each of the five wavelengths by calculating the emergent intensity distribution on the plane of the sky and convolving it with the instrumental point spread function (PSF)[2] at the particular wavelength. The parameters are then adjusted to obtain an inverse-variance weighted least-squares fit to the observed images.

In this procedure, the wavelength variation of opacity is assumed to be given by equation (1), and the radial variations of volume density and dust temperature are assumed to be described by Plummer-like (Plummer 1911) and quadratic forms, respectively. Specifically, we use

$$n(r) = n_0/[1 + (r/r_0)^\alpha] \tag{2}$$

$$T(r) = T_0 + (T_1 - T_0 - T_2)r/r_{out} + T_2(r/r_{out})^2, \tag{3}$$

where $n(r)$ represents the number density of H_2 molecules at radial distance r, r_0 represents the radius of an inner plateau and r_{out} is the outer radius of the core, outside of which the core density is assumed to be zero. Also, T_0 is the central core temperature, T_1 is the temperature at the outer radius and T_2 is a coefficient which determines the curvature of the radial temperature profile. In relating $n(r)$ to the corresponding profile of mass density, we assume a mean molecular weight of 2.8 (Roy et al. 2013).

The set of unknowns then consists of n_0, r_0, r_{out}, α, T_0, T_1, T_2, x, y, where the latter two variables represent the angular coordinates of the core centre. Representing this set by a nine-component parameter vector, $\boldsymbol{p}$, we can write the measurement model as

$$\boldsymbol{\zeta}_\lambda = \boldsymbol{f}_\lambda(\boldsymbol{p}) + b_\lambda + \boldsymbol{v}_\lambda, \tag{4}$$

where $\boldsymbol{\zeta}_\lambda$ is a vector representing the set of pixels of the observed image at wavelength λ, $\boldsymbol{f}_\lambda(\boldsymbol{p})$ represents the model core image for parameter set $\boldsymbol{p}$ and $\boldsymbol{v}_\lambda$ is the measurement noise vector, assumed to be an uncorrelated zero-mean Gaussian random process. Also, b_λ represents the local background level, estimated using the histogram of pixel values in an annulus[3] surrounding the source. This measurement model assumes implicitly that the core is optically thin at all wavelengths of observation.

In principle, the solution procedure is then to minimize the chi-squared function, $\phi(\boldsymbol{p})$, given by

$$\phi(\boldsymbol{p}) = \sum_{\lambda,i}[(\boldsymbol{\zeta}_\lambda)_i - b_\lambda - (\boldsymbol{f}_\lambda(\boldsymbol{p}))_i]^2/\sigma_\lambda^2, \tag{5}$$

where subscript i refers to the ith pixel of the image at the given wavelength and σ_λ represents the standard deviation of the measurement errors, evaluated from the sky background fluctuations in the background annulus.

In practice, two difficulties arise.

---

[2] For the PACS images, we use azimuthally averaged versions of the PSFs estimated from observations of Vesta (Lutz 2012); for SPIRE we use rotationally symmetric PSFs based on the measured radial profiles presented by Griffin et al. (2013).

[3] The inner radius of this annulus is taken as the size of the source 'footprint' which is estimated by *getsources* and includes all of the source emission on the observed images; the outer radius is set 10 per cent larger.

Table 1. Results of testing with synthetic data.

Model	T_0 (K)			Mass ($M_\odot$)			Peak H_2 col. dens. (10^{22} cm^{-2})		
	Std.[a]	Alt.[b]	True	Std.	Alt.	True	Std.	Alt.	True
1	10.1	8.6	10.0	0.61	0.39	0.59	0.59	0.45	1.04
2	6.8	6.5	6.5	22.7	9.48	18.4	23.9	5.65	16.1
3	7.8	6.5	6.7	3.30	1.46	3.11	7.95	4.91	13.4

[a]Standard version of COREFIT.
[b]Alternate version (COREFIT-PH).

(i) An unconstrained minimization of $\phi(\boldsymbol{p})$ is numerically unstable due to the fact that for a given total number of molecules, n_0 in equation (2) becomes infinite as $r_0 \rightarrow 0$. It results in near-degeneracy such that the data do not serve to distinguish between a large range of possible values of the central density. To overcome this, we have modified the procedure to incorporate the constraint $r_0 \geq r_{\min}$, where $r_{\min}$ is equal to one quarter of the nominal angular resolution, which we take to be the beamwidth at 250 μm. The estimate of central density then becomes a 'beam-averaged' value over a resolution element of area $\pi r_{\min}^2$. For a distance of 140 pc, $r_{\min}$ corresponds to about 600 au.

(ii) Most cores show some degree of asymmetry. This can degrade the quality of the global fit to a spherically symmetric model, causing the centre of symmetry to miss the physical centre of the core. Some negative consequences include an underestimate of the central density and an overestimate of the central temperature. To alleviate this, we estimate the (x, y) location of the core centre ahead of time using the peak of a column density map, constructed at the spatial resolution of the 250 μm image. The maximum likelihood estimation is then carried out using a seven-component parameter vector which no longer involves the positional variables.

Having performed the position estimation and constrained chi-squared minimization, the core mass is then obtained by integrating the density profile given by equation (2), evaluated using the estimated values of n_0, r_0 and α.

Evaluation of the uncertainties in parameter estimates is complicated by the non-linear nature of the problem which leads to a multiple-valley nature of $\phi(\boldsymbol{p})$. The usual procedure, in which the uncertainty is evaluated by inverting a matrix of second derivatives of $\phi(\boldsymbol{p})$ (Whalen 1971), then only provides values which correspond to the width of the global maximum and ignores the existence of neighbouring peaks which may represent significant probabilities. We therefore evaluate the uncertainties using a Monte Carlo technique in which we repeat the estimation procedure after adding a series of samples of random noise to the observational data and examine the effect on the estimated parameters.

We have also implemented an alternate version of COREFIT, referred to as 'COREFIT-PH', in which the dust temperature profile is based on a radiative transfer model, PHAETHON (Stamatellos & Whitworth 2003), rather than estimating it from the observations. In this model, the radial density profile has the same form as for the standard COREFIT (equation 2) but with the index, α, fixed at 2. The temperature profile is assumed to be determined entirely by the heating of dust by the external ISRF; the latter is modelled locally as a scaled version of the standard ISRF (Stamatellos, Whitworth & Ward-Thompson 2007) using a scaling factor, χ_{ISRF}, which represents an additional variable in the maximum likelihood solution. We now compare the results obtained using the two approaches, both for synthetic and real data.

5.1 Tests with synthetic data

We have tested both COREFIT and COREFIT-PH against synthetic data generated using an alternate forward model for dust radiative transfer, namely MODUST (Bouwman et al., in preparation). Using the latter code, images at the five wavelengths were generated for a set of model cores and convolved with Gaussian simulated PSFs with full width at half-maxima corresponding to the *Herschel* beamsizes. The models involved central number densities of 10^5, 10^6 and 3×10^6 cm^{-3} with corresponding r_0 values of 2500, 4000 and 1000 au, respectively, and r_{out} values of 1.3×10^4, 1.7×10^4 and 1.2×10^4 au, respectively. The corresponding core masses were 0.59, 18.37 and 3.11 $M_\odot$, respectively. The synthesized images and corresponding Gaussian PSFs were then used as input data to the inversion algorithms. The results are presented in Table 1.

It is apparent that COREFIT gave masses and central temperatures in good agreement with the true model. While COREFIT-PH reproduced the central temperatures equally well, it underestimated the masses of these simulated cores by factors of 0.7, 0.5 and 0.5, respectively. The reason for these differences is that even though the two radiative transfer codes (PHAETHON and MODUST) yield central temperatures in good agreement with each other for a given set of model parameters, they produce divergent results for the dust temperatures in the outer parts of the cores, due largely to differences in dust model opacities. Since the outer parts comprise a greater fraction of the mass than does the central plateau region, this can lead to substantially different mass estimates given the same data. This problem does not occur for COREFIT since the latter obtains the temperature largely from the spectral variation of the data rather than from a physical model involving additional assumptions. These calculations thus serve to illustrate the advantages of simultaneous estimation of the radial profiles of dust temperature and density.

5.2 Results obtained with observational data

Table 2 shows the complete set of COREFIT parameter estimates for each of the Taurus cores. Also included are the assumed values of the inner radius of the annulus used for background estimation, equal to the *getsources* footprint size. Table 3 shows a comparison of the mass and temperature estimates amongst the different techniques, which include COREFIT and COREFIT-PH as well as the SED fitting discussed in Section 3. To facilitate comparison between the COREFIT temperatures and the mean core temperatures estimated from the spatially integrated fluxes used in the SED fits, we include the spatially averaged COREFIT temperature, $\bar{T}$, defined as the density-weighted mean value of $T(r)$ for $r \leq r_{\text{out}}$. The COREFIT-PH results include the values of the ISRF scaling factor, χ_{ISRF}, the median value of which is 0.33. The fact that this is noticeably less than unity can probably be attributed to the fact that these cores are all embedded in filaments and hence the local ISRF is attenuated by overlying filamentary material. As an example of the fitting results,

Table 2. COREFIT parameter estimates for the 20 Taurus cores.

Core No.	RA (J2000)	Dec. (J2000)	$r_{annulus}$[a] (10^3 AU)	r_0 (10^3 AU)	r_{out} (10^3 AU)	n_0 (10^5 cm^{-3})	α[b]	T_0[c] (K)	T_1 (K)	T_2[d] (K)
1	04:13:35.8	+28:21:11	7.56	3.5 ± 1.2	7.1 ± 0.2	0.5 ± 0.1	2.0 ± 0.6	9.5 ± 0.5	11.2 ± 0.1	−1.4 ± 0.6
2	04:17:00.6	+28:26:32	16.38	4.7 ± 0.2	13.2 ± 0.6	0.7 ± 0.1	3.1 ± 0.4	10.7 ± 0.3	12.5 ± 0.2	−1.2 ± 0.2
3	04:17:32.3	+27:41:27	11.20	3.5 ± 3.1	7.3 ± 0.4	0.2 ± 0.1	2.0 ± 1.0	12.3 ± 0.8	13.1 ± 1.2	0.2 ± 0.1
4	04:17:35.2	+28:06:36	10.30	8.4 ± 0.4	8.4 ± 0.4	9.9 ± 2.9	3.7 ± 0.2	7.1 ± 0.6	23.7 ± 1.2	−2.6 ± 0.5
5	04:17:36.2	+27:55:46	13.20	2.9 ± 1.0	11.8 ± 0.4	0.8 ± 0.3	2.6 ± 0.4	9.4 ± 0.4	12.0 ± 0.3	−2.3 ± 0.5
6	04:17:41.8	+28:08:47	10.08	0.8 ± 0.2	8.8 ± 1.2	26 ± 18	2.0 ± 0.4	7.0 ± 0.1	8.3 ± 0.4	−1.1 ± 0.3
7	04:17:43.2	+28:05:59	7.14	1.0 ± 0.4	6.9 ± 0.2	13 ± 6	2.6 ± 0.3	7.1 ± 0.4	10.1 ± 0.2	−2.9 ± 0.5
8	04:17:49.4	+27:50:13	8.10	2.9 ± 2.9	7.7 ± 0.2	0.5 ± 0.2	1.9 ± 1.8	9.9 ± 1.6	10.8 ± 0.5	0.9 ± 0.6
9	04:17:50.6	+27:56:01	13.86	4.5 ± 0.2	10.4 ± 0.4	1.9 ± 0.1	3.4 ± 0.6	8.0 ± 0.2	10.1 ± 0.2	−1.0 ± 0.2
10	04:17:52.0	+28:12:26	12.60	4.3 ± 1.7	11.2 ± 0.2	0.9 ± 0.4	2.2 ± 0.6	10.0 ± 0.6	9.7 ± 0.6	−0.1 ± 0.3
11	04:17:52.5	+28:23:43	12.15	2.1 ± 1.0	9.5 ± 0.2	1.0 ± 0.3	1.9 ± 0.4	9.8 ± 0.6	11.2 ± 0.3	−0.4 ± 0.2
12	04:18:03.8	+28:23:06	8.75	2.3 ± 0.6	8.6 ± 0.2	2.3 ± 0.4	3.0 ± 0.9	9.9 ± 1.1	10.8 ± 1.1	0.9 ± 0.7
13	04:18:08.4	+28:05:12	13.86	2.3 ± 0.8	13.4 ± 0.2	6.8 ± 1.8	2.8 ± 0.4	6.0 ± 0.5	11.4 ± 0.3	−3.2 ± 0.5
14	04:18:11.5	+27:35:15	7.45	2.3 ± 1.4	7.3 ± 0.2	1.9 ± 0.5	2.0 ± 0.5	7.8 ± 0.4	10.1 ± 0.3	−2.2 ± 0.7
15	04:19:37.6	+27:15:31	11.76	2.7 ± 0.6	10.7 ± 0.4	1.6 ± 0.4	2.0 ± 0.2	8.8 ± 0.4	10.6 ± 0.1	−1.5 ± 0.2
16	04:19:51.7	+27:11:33	9.24	3.1 ± 0.4	8.9 ± 0.2	3.9 ± 0.5	3.4 ± 0.7	6.4 ± 0.2	9.6 ± 0.3	−3.0 ± 0.5
17	04:20:02.9	+28:12:26	10.30	1.4 ± 0.4	10.0 ± 0.4	0.5 ± 0.3	2.0 ± 0.3	10.7 ± 0.4	12.7 ± 0.2	−1.9 ± 0.5
18	04:20:52.5	+27:02:20	5.30	5.2 ± 2.9	5.2 ± 0.2	0.3 ± 0.1	indet.	11.4 ± 0.9	11.3 ± 0.4	0.1 ± 0.4
19	04:21:06.8	+26:57:45	8.10	2.7 ± 1.2	4.7 ± 0.6	0.6 ± 0.2	3.0 ± 1.2	11.1 ± 0.6	11.8 ± 0.2	0.1 ± 0.0
20	04:21:12.0	+26:55:51	8.75	2.9 ± 0.8	8.6 ± 0.2	0.3 ± 0.1	4.0 ± 1.2	10.1 ± 0.7	13.9 ± 0.1	−1.6 ± 0.6

[a]Inner radius of the annulus used for background estimation.
[b]An entry of 'indet.' indicates that α is indeterminate from the data; this occurs if $r_0 \simeq r_{out}$.
[c]Central core temperature, effectively an average over a resolution element of radius $r_{min} = 600$ au.
[d]Negative values of T_2 indicate negative curvature of the temperature profile and have no correspondence with actual temperatures.

Table 3. Comparison of masses and temperatures estimated using the three different techniques discussed in the text.

	SED fitting[a]		COREFIT			COREFIT-PH		
Core no.	Mass (M$_\odot$)	T (K)	Mass (M$_\odot$)	T_0 (K)	$\bar{T}$[b] (K)	Mass (M$_\odot$)	T_0 (K)	χ_{ISRF}[c]
1	1.19 ± 0.05	9.9 ± 0.3	0.20 ± 0.01	9.5 ± 0.5	10.8	0.25	8.2	0.28
2	0.71 ± 0.04	11.8 ± 0.5	0.84 ± 0.04	10.7 ± 0.3	11.8	0.72	8.4	0.90
3	0.10 ± 0.01	12.3 ± 0.5	0.09 ± 0.04	12.3 ± 0.8	12.7	0.23	9.1	0.37
4	0.05 ± 0.01	12.6 ± 0.8	0.04 ± 0.01	7.1 ± 0.6	9.3	0.08	9.1	0.29
5	0.20 ± 0.01	11.3 ± 0.1	0.37 ± 0.02	9.4 ± 0.4	10.9	0.32	8.0	0.37
6	1.01 ± 0.15	8.0 ± 0.6	1.70 ± 0.34	7.0 ± 0.1	7.7	1.64	5.0	0.26
7	0.22 ± 0.10	8.8 ± 1.1	0.49 ± 0.04	7.1 ± 0.4	8.6	0.37	6.0	0.31
8	0.07 ± 0.01	9.9 ± 1.5	0.19 ± 0.04	9.9 ± 1.6	10.3	0.25	6.7	0.14
9	1.53 ± 0.02	9.2 ± 0.1	1.44 ± 0.09	8.0 ± 0.2	9.2	1.53	5.5	0.39
10	1.30 ± 0.20	8.8 ± 0.9	0.96 ± 0.02	10.0 ± 0.6	9.9	1.35	5.8	0.32
11	0.20 ± 0.03	11.8 ± 1.1	0.32 ± 0.06	9.8 ± 0.6	10.6	0.41	7.4	0.29
12	0.42 ± 0.05	9.2 ± 0.6	0.41 ± 0.06	9.9 ± 1.1	10.1	0.40	6.6	0.39
13	1.60 ± 0.28	8.8 ± 1.0	2.03 ± 0.16	6.0 ± 0.5	8.3	2.21	5.4	0.32
14	0.47 ± 0.11	8.8 ± 1.7	0.46 ± 0.05	7.8 ± 0.4	9.4	0.33	6.7	0.25
15	0.21 ± 0.07	11.2 ± 1.9	0.84 ± 0.08	8.8 ± 0.4	10.0	1.04	6.1	0.36
16	0.36 ± 0.06	8.7 ± 0.5	1.08 ± 0.12	6.4 ± 0.2	8.3	1.52	5.0	0.26
17	0.05 ± 0.01	12.5 ± 1.2	0.08 ± 0.01	10.7 ± 0.4	11.9	0.12	8.8	0.18
18	0.21 ± 0.03	9.6 ± 0.8	0.09 ± 0.02	11.4 ± 0.9	11.3	0.07	9.2	0.25
19	0.08 ± 0.01	11.8 ± 0.8	0.08 ± 0.02	11.1 ± 0.6	11.5	0.09	8.6	0.38
20	0.02 ± 0.01	13.6 ± 0.7	0.06 ± 0.01	10.1 ± 0.7	11.8	0.05	10.2	0.28

[a]Based on spatially integrated fluxes.
[b]Density-weighted mean value of $T(r)$ for $r \leq r_{out}$.
[c]Estimated ISRF scaling factor.

Figs 2 and 3 show the estimated density and temperature profiles for core no. 2 in Table 2, based on COREFIT and COREFIT-PH, respectively.

Fig. 4 shows that the two techniques yield consistent estimates of masses, but the radiative transfer calculations produce central temperatures which are, on average, ∼2 K lower than the COREFIT estimates. Although the difference is not significant in individual cases (the standard deviation being 1.4), it is clear from Fig. 4 that a systematic offset is present; the mean temperature difference, ΔT, is 1.9 ± 0.3 K.

Based on the results of testing with synthetic data, this difference seems too large to be explained by systematic errors associated
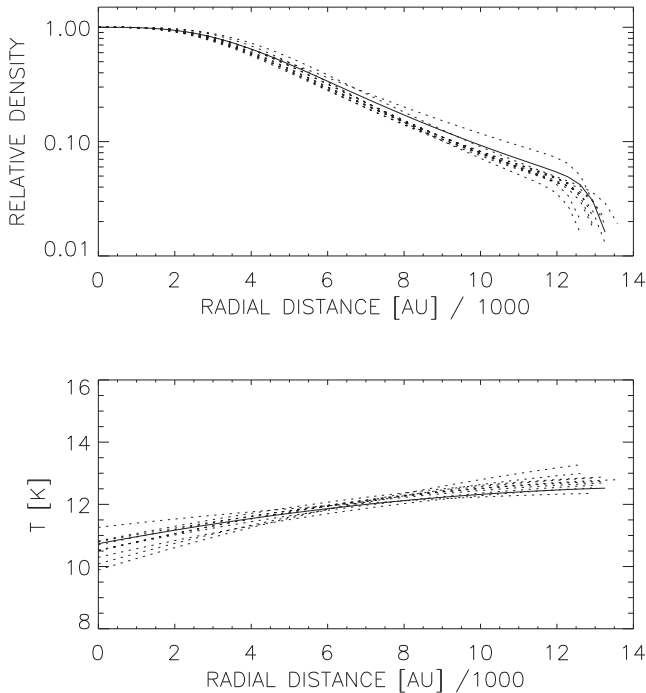
Figure 2. Example of COREFIT results, for a 0.7 M$_\odot$ core in L1495 (no. 2 in Table 2). The solid lines indicate maximum likelihood estimates of the profiles of relative volume density and dust temperature. The dashed lines provide a measure of the uncertainty in the estimated density and temperature. They represent the results of a Monte Carlo simulation in which the estimation procedure is repeated 10 times after adding synthetic measurement noise to the observed images; the standard deviation of the added noise corresponds to the estimated measurement noise of the observed images.
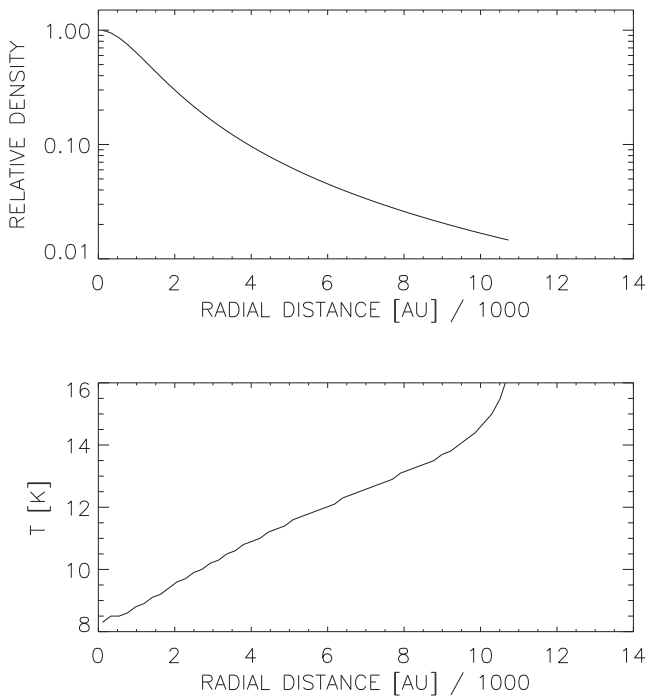
Figure 3. COREFIT-PH results for the same core as in Fig. 2. In this variant of the estimation procedure, the dust temperature profile is modelled using a radiative transfer code (PHAETHON) instead of estimating it from the observations.
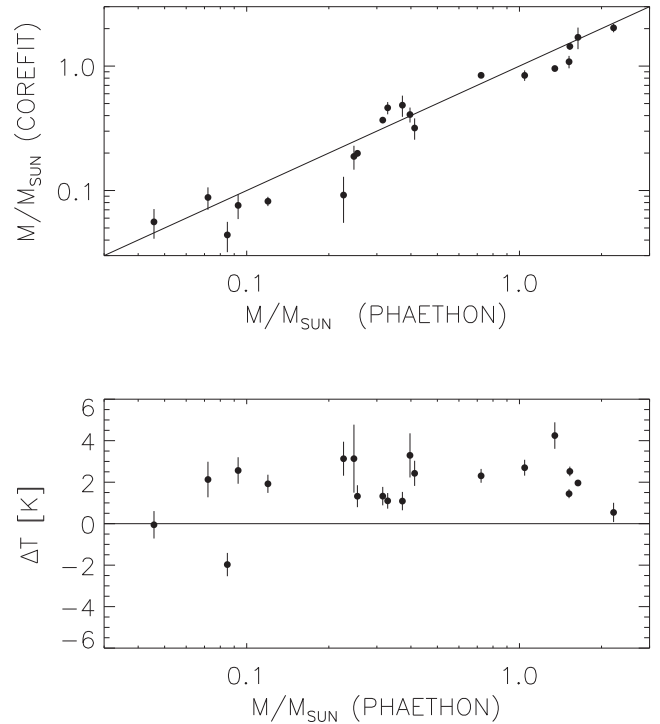
Figure 4. Comparison between parameter estimates, obtained using COR-EFIT and COREFIT-PH, for the 20 selected cores. In the former procedure, the dust temperature profile is estimated directly from the observations, while in the latter it is modelled using radiative transfer. Upper plot: CORE-FIT mass versus COREFIT-PH mass. For reference, the solid line represents the locus of equal masses. Lower plot: ΔT versus mass, where ΔT represents the difference in estimated temperature (COREFIT minus COREFIT-PH).

with dust grain models, although we cannot rule out that possibility. One could also question whether our χ_{ISRF} values are spuriously low. We do, in fact, find that by forcing the latter parameter to a somewhat larger value (0.5), the median ΔT can be reduced to zero with only a modest increase in the reduced chi-squared, χ_ν^2 (0.85 as opposed to 0.83 for the best fit). The observations are completely inconsistent with $\chi_{ISRF} = 1.0$, however. As an additional test, we can take the COREFIT estimate of the radial density distribution for each core and use the stand-alone PHAETHON code to predict the central temperature for any assumed value of χ_{ISRF}. We thereby obtain consistency with the COREFIT estimates with $\chi_{ISRF} = 0.67$. However, this consistency comes at significant cost in terms of goodness of fit (the median χ_ν^2 increases to 2.27), and therefore does *not* serve to reconcile the COREFIT results with the expectations of radiative transfer. In summary, the COREFIT results are not entirely consistent with our assumed model for dust heating by the ISRF, but further work will be necessary to determine whether the differences are model related or have astrophysical implications. So at this stage we have no evidence to contradict the findings of Evans et al. (2001), who considered various heating sources (the primary and secondary effects of cosmic rays and heating of dust grains by collisions with warmer gas particles) and concluded that heating by the ISRF dominates over all other effects.

How do the COREFIT estimates of temperature and mass compare with the preliminary values estimated from the *getsources* SEDs? In the case of temperature, the relevant comparison is between the SED-derived value and the spatially averaged COREFIT value; the data in Table 3 then give a mean 'COREFIT minus SED' difference of −0.2 K, with a standard deviation of 1.1 for individual
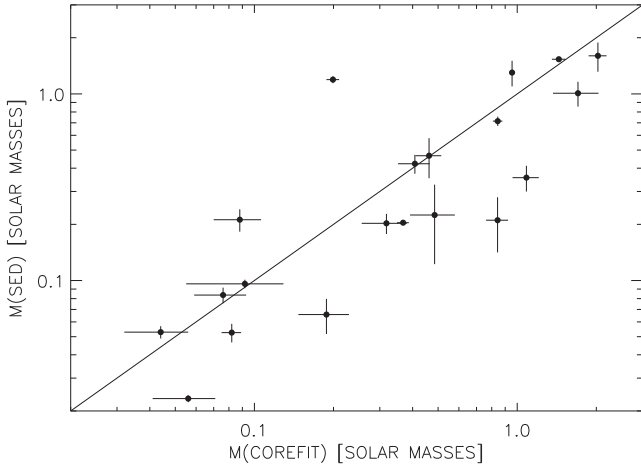
Figure 5. SED-derived mass based on isothermal assumption versus the mass from COREFIT model. For reference, the solid line represents the locus of equal masses.
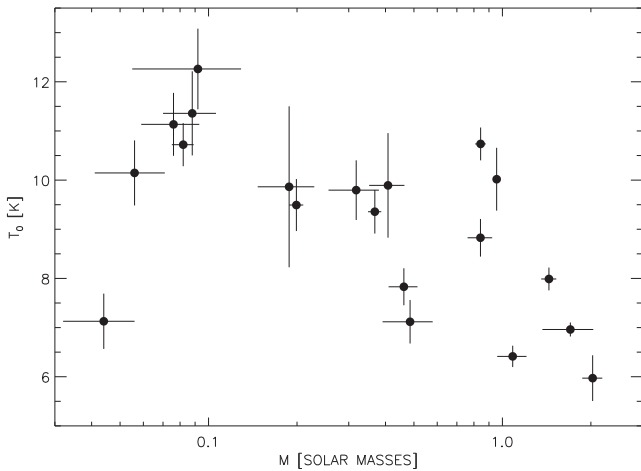

Figure 7. Central dust temperature, T_0, as a function of peak column density of H_2 molecules.

Figure 6. Central dust temperature, T_0, as a function of core mass.
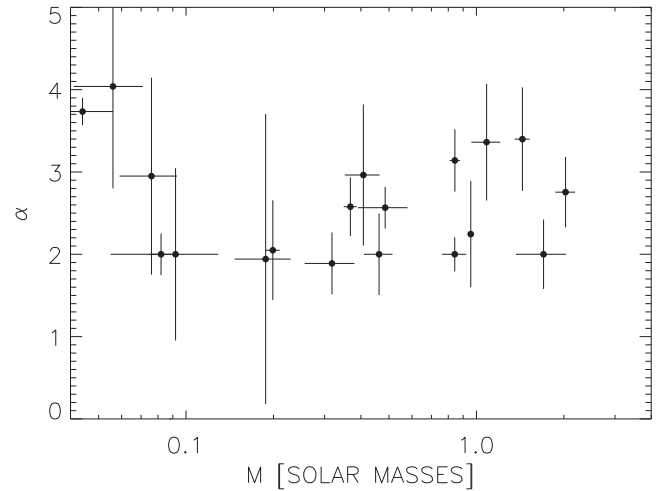
Figure 8. The estimated index of radial density falloff, α, as a function of core mass.

cores. The temperature estimates are thus consistent. With regard to mass, Fig. 5 shows that SED fitting under the isothermal assumption yields masses that are systematically smaller than the COREFIT values; the mean ratio of COREFIT mass to SED-based mass is 1.5, with a standard deviation of 1.0 in individual cases. Since the internal temperature gradient increases with the core mass, one might expect that the correction factor for SED-derived masses would increase with mass, although Fig. 5 has too much scatter to establish this. It may be evident when the results are averaged for a much larger statistical sample of cores, although the correction may well depend on environmental factors such as the intensity of the local ISRF.

Fig. 6 shows a plot of estimated central temperature as a function of core mass. Linear regression indicates that these quantities are negatively correlated with a coefficient of −0.64. This correlation can be explained quite naturally as a consequence of increased shielding of the core, from the ISRF, with increasing core mass. This being the case, one would expect an even stronger correlation with peak column density and this is confirmed by Fig. 7, for which the associated correlation coefficient is −0.86.

Fig. 8 shows a plot of α versus mass, where α is the index of radial density variation as defined by equation (2) and the masses are the COREFIT values. Given the relatively large uncertainties,
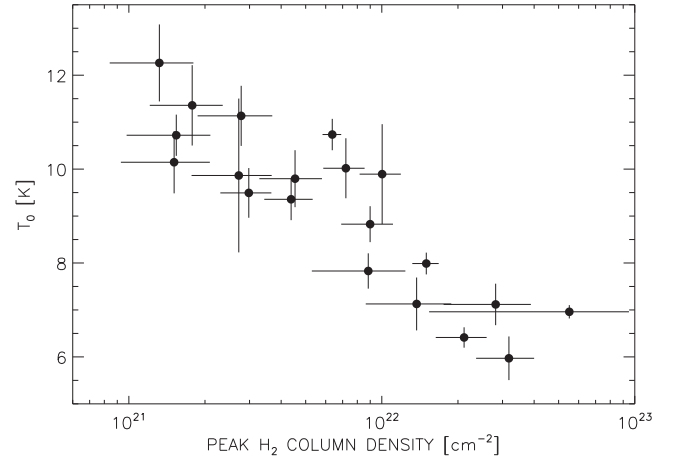
the α values are, for the most part, consistent with values expected for Bonnor–Ebert spheres, whereby $\alpha = 2.5$ provides an accurate empirical representation at radial distances up to the instability radius (Tafalla et al. 2004), and that α decreases to its asymptotic value of 2 beyond that.

The general consistency with the Bonnor–Ebert model is supported by the fact that when the maximum likelihood fitting procedure is repeated using the constraint $\alpha = 2$, the chi-squared values are, in most cases, not significantly different from the values obtained when α is allowed to vary. Two exceptions, however, are cores 2 and 13, both of which are fitted significantly better by density profiles steeper than Bonnor–Ebert ($\alpha = 3.1$ and 2.8, respectively), as illustrated by Fig. 9 for the former case. Specifically, the chi-squared[4] differences (17.2 and 7.5, respectively) translate into relative probabilities, for the '$\alpha = 2$' hypothesis, of $\sim 2 \times 10^{-4}$ and 0.02, respectively. If confirmed, such behaviour may have some important implications for core collapse models; a steepening of the

---

[4] To evaluate this quantity, the number of degrees of freedom, N_{df}, was taken as the total number of resolution elements contained within the fitted region for all five input images; N_{df} is then ~ 1700 and ~ 1200 for the two cases, respectively.
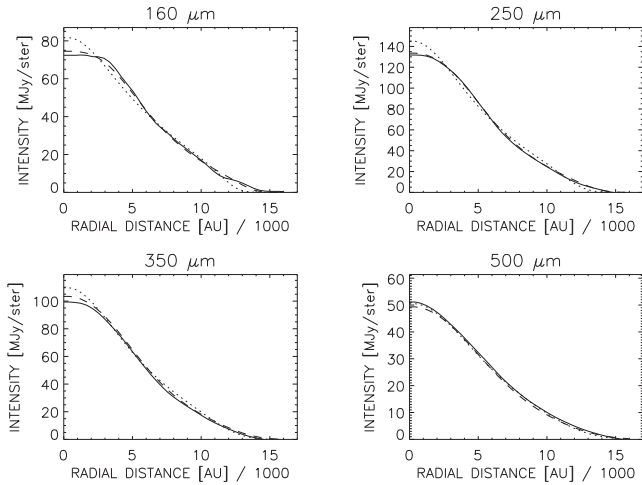
Figure 9. Radial profiles of the images of core no. 2 at four wavelengths, showing the match between observations and models for two different values of the radial density index, α. Solid line: observed profile; dashed line: best-fitting model ($\alpha = 3.1$) convolved with the corresponding PSF at each wavelength); dotted line: same, except for the constraint $\alpha = 2.0$. Note that the latter model results in a poor fit in the central region.

density distribution in the early collapse phase is, in fact, predicted by the model of Vorobyov & Basu (2005) in which the collapsing core begins to detach from its outer boundary.

6 CORE STABILITY

Assessments of core stability are frequently made using SED-based estimates of core mass and temperature and observed source size, assuming that cores are isothermal and can be described as Bonnor–Ebert spheres (Lada et al. 2008). Using the SED-based data in Table 3 in conjunction with the *getsources* estimates of core size, we thereby find that the estimated core mass exceeds the Bonnor–Ebert critical mass for 10 of our 20 cores, suggesting that half of our cores are unstable to gravitational collapse.

Our COREFIT parameter estimates enable us to make a more detailed assessment of core stability based on a comparison with the results of hydrostatic model calculations that take account of the non-isothermal nature of the cores. This is facilitated by the modified Bonnor–Ebert (MBE) sphere models of Sipilä, Harju & Juvela (2011). Adopting their model curves, based on the Li & Draine (2001) grains which best reproduce our estimated core temperatures, the locus of critical non-isothermal models on a density versus mass plot is shown by the solid line in Fig. 10. Also plotted in this figure, for comparison, are the COREFIT estimates of those quantities. The seven points to the right of this curve represent cores that we would consider to be gravitationally unstable based on the MBE models. Although this is somewhat less than the 10 that were classified as unstable based on the SED fits, the difference is probably not significant given that several points on the plot lie close to the 'stability' line.

The consistency between the above two procedures for stability assessment is illustrated by the fact that the MBE stability line in Fig. 10 provides a fairly clean demarcation between the cores classified as stable (open circles) and unstable (filled circles) from the simpler (SED-based) procedure. These results therefore suggest that prestellar cores can be identified reliably as such using relatively simple criteria.
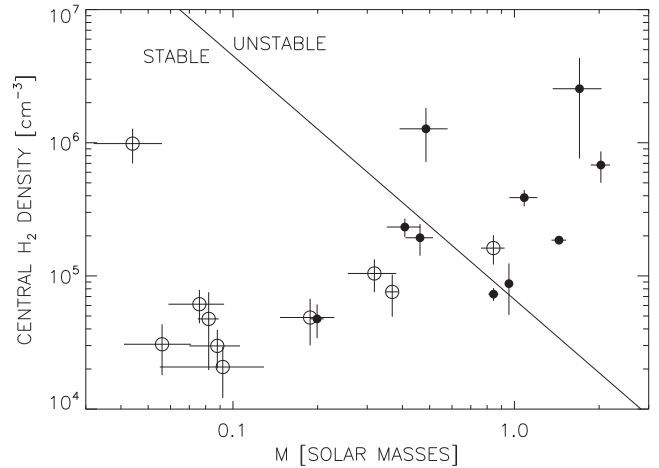

Figure 10. Central number density of H_2 molecules as a function of core mass. The circles represent the COREFIT estimates for L1495; filled symbols designate the subset of cores whose preliminary assessment of dynamical status suggests that they are gravitationally bound, based on *getsources* fluxes and sizes in conjunction with the standard model of isothermal Bonnor–Ebert spheres. For comparison, the solid line represents the locus of critically stable non-isothermal Bonnor–Ebert spheres (Sipilä, Harju & Juvela 2011); points to the right of this line represent cores which are unstable to gravitational collapse according to that model.

The Bonnor–Ebert model also provides a stability criterion with respect to the centre-to-edge density contrast, whereby values greater than 14 indicate instability to gravitational collapse, both for the isothermal and non-isothermal cases (Sipilä et al. 2011). However, the outer boundaries are not well defined for the present sample of cores, and consequently the contrast values are uncertain in most cases. Two exceptions are cores 2 and 13, both of which have contrast estimates whose significance exceeds 3σ. In both cases, the mass exceeds the Bonnor–Ebert critical mass (by ratios of 1.2 and 6.0, respectively), and the centre-to-edge contrast values (20 ± 6 and 104 ± 32, respectively) are in excess of 14. So for those two cores, at least, the core stability deduced from the density contrast is thus consistent with that assessed from total mass.

7 COMPARISON WITH PREVIOUS OBSERVATIONS

The deduced physical properties of our cores may be compared with previously published spectral line data in $H^{13}CO^+$ and N_2H^+, both of which are known to be good tracers of high-density gas ($n(H_2) \gtrsim 10^5$ cm^{-3}). Of our 20 cores, we find accompanying observations for 10 in $H^{13}CO^+$ (Onishi et al. 2002) and 7 in N_2H^+ (Hacar et al. 2013). The relevant parameters are given in Table 4.

Considering first the $H^{13}CO^+$ data, comparison of observed peak locations with dust continuum source positions from COREFIT shows a distinct lack of detailed correspondence. This behaviour is apparent in Fig. 1 and from Table 4 which includes the angular distance (labelled as 'Offset' in the table) between each of the $H^{13}CO^+$ source locations and the corresponding dust continuum core location. The median distance is 59 arcsec, considerably larger than the spatial resolution of either the $H^{13}CO^+$ observations (20 arcsec) or the *Herschel* data (18 arcsec at 250 μm). These offsets are somewhat surprising, since previous comparisons between $H^{13}CO^+$ and dust continuum maps have shown good correspondence (Umemoto et al. 2002). One could question whether they are due to gridding errors in the $H^{13}CO^+$ data, in view of the fact that the observations

were made on a relatively coarse grid [the eight cores of Onishi et al. (2002) in Table 4 are split evenly between 30 and 60 arcsec grid spacings]. However, the measured offsets show no correlation with the grid spacing – the mean offset is approximately 50 arcsec in either case; this argues against gridding error as an explanation. The most likely reason for the systematic offsets is that the $H^{13}CO^+$ is frozen out at the low ($\lesssim 10$ K) temperatures of the core centres (Walmsley et al. 2004).

Detailed comparison of the dust continuum core locations with the $H^{13}CO^+$ maps (four examples of which are given in Fig. 11) shows that the majority of sources are elongated and/or double and that in some cases (Onishi core no. 3 in particular) the dust continuum source falls between the pair of $H^{13}CO^+$ components. In other cases (e.g. Onishi core no. 16a), the dust continuum peak falls on a nearby secondary maximum of the $H^{13}CO^+$ emission. In the latter case, surprisingly, the main peak of $H^{13}CO^+$ falls in a local *minimum* of dust emission. Comparisons between $H^{13}CO^+$ images and their 250 μm counterparts show that, in general, the elongation and source alignment in $H^{13}CO^+$ is along the filament, so we have a rod-like, rather than spherical, geometry. The picture which thus emerges is that when a core forms in a filament (André et al. 2010), we see the core centre in dust continuum emission and the warmer (but still dense, $\sim 10^5$ cm^{-3}) $H^{13}CO^+$ gas on either side of it in a dumbbell-like configuration. The median separation of the dust continuum and $H^{13}CO^+$ sources then corresponds to the typical radius of the depletion zone. For an ensemble of randomly oriented filaments, the mean projected separation is $\pi/4$ times the actual separation, which means that our estimated median separation of 59 arcsec corresponds to an actual separation of 75 arcsec, or about 1.1×10^4 au at the distance of L1495. This is similar to the radius of the dark-cloud chemistry zone in which carbon-bearing molecules become gaseous (Caselli 2011).

Comparing the estimated masses, Table 4 shows that the values estimated from dust continuum observations are, in most cases, much smaller than those based on $H^{13}CO^+$. The discrepancy ranges from a factor of ~ 2 to more than an order of magnitude. Based on the mass and positional discrepancies, it is clear that $H^{13}CO^+$ and submillimetre continuum are not mapping the same structures.
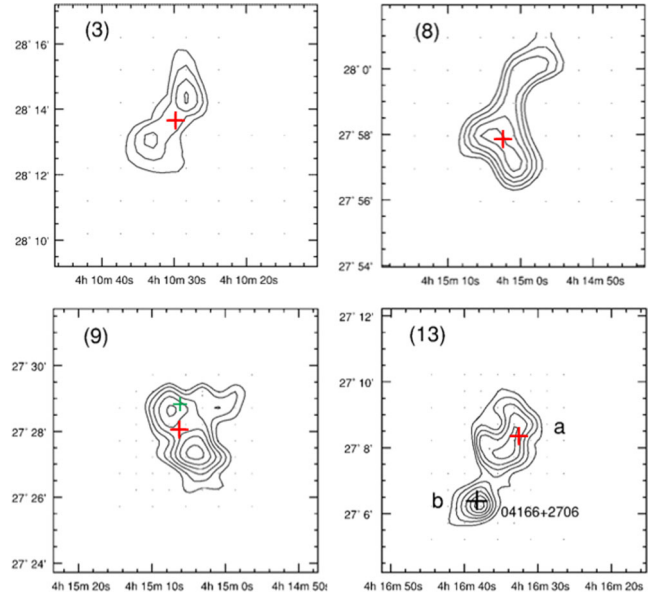

Figure 11. Examples of dust continuum core locations in relation to $H^{13}CO^+$ emission. The estimated locations of cores 1, 13, 14 and 15 (corresponding to Onishi core nos. 3, 8, 9 and 13a, respectively) are superposed on $H^{13}CO^+$ maps taken from Onishi et al. (2002) (B1950 coordinates). In each case, the location of peak dust column density is indicated by a red cross. The green cross in Onishi field (9) represents a secondary peak of dust emission. The black cross in Onishi field (13) represents a protostar location.

Nevertheless, it remains to explain why so much of the expected dust emission from the $H^{13}CO^+$ emitting gas is apparently not being seen in the submillimetre continuum. It is unlikely to be a result of the background subtraction in COREFIT since the COREFIT mass estimates match the SED-based values from *getsources* fluxes within ~ 30 per cent and the only background that was subtracted during the latter processing corresponded to the natural spatial scale of the broader underlying emission structure.

Table 4. Comparison with previously published spectral line data.

Core[a] no.	ID[b] Onishi	Hacar	Offset[c] (arcsec) $H^{13}CO^+$	N_2H^+	Dust[e]	Radius (pc) $H^{13}CO^+$	N_2H^+	Mass (M$_\odot$)[d] Dust	$H^{13}CO^+$	n(H$_2$) (10^5 cm^{-3}) Dust	$H^{13}CO^+$
1	3	–	41	–	0.034	0.021	–	0.2	1.7	0.5	0.9
4	5	–	74	–	0.041	0.054	–	0.04	6.5	9.8	1.9
6	5	1	93	43	0.043	0.054	0.048	1.7	6.5	25	1.9
7	5	–	91	–	0.034	0.054	–	0.5	6.5	13	1.9
9	–	2	–	8.4	0.050	–	0.027	1.4	–	1.9	–
10	6	–	52	–	0.054	0.034	0.051	1.0	5.8	0.9	1.2
12	7	5	82	31	0.042	0.035	0.030	0.4	2.9	2.3	1.9
13	8	6	24	44	0.065	0.064	0.053	2.0	5.0	6.8	1.0
14	9	7	44	21	0.035	0.060	–	0.5	4.2	1.9	1.0
15	13a	10	8.0	19	0.052	0.048	0.047	0.8	3.4	1.6	1.4
16	–	12	–	9.4	0.043	–	0.034	1.1	–	3.9	–
18	16a	–	59	–	0.025	0.028	–	0.09	3.0	0.3	2.5

[a] As listed in Table 2.
[b] Object number in previously published source lists: Onishi et al. (2002) in $H^{13}CO^+$, and Hacar et al. (2013) in N_2H^+.
[c] Angular offset from the COREFIT (dust continuum) position.
[d] The mass quoted in the 'Dust' column represents the COREFIT estimate of total mass (gas + dust) based on the dust thermal continuum in the 70–500 μm range; the mass quoted for $H^{13}CO^+$ represents a virial mass derived by Onishi et al. (2002).
[e] The radius quoted here is $r_{\rm out}$ from Table 2, converted to pc.

The most likely explanation for the discrepancy is an overestimation of the virial mass of the gas component due, in part, to the assumption by Onishi et al. (2002) of uniform velocity dispersion. Specifically, the velocity dispersion of the relatively cool gas being probed by dust emission is likely to be at least a factor of 2 lower than that of $H^{13}CO^+$, as suggested by the N_2H^+ observations of Hacar et al. (2013), and since the estimated virial mass depends on the square of that dispersion, it could have been overestimated by a factor of up to 4. Two additional effects, both of which are likely to have led to overestimation of the virial mass are as follows:

(i) the Onishi et al. (2002) virial mass was based on assumed spherical shape as opposed to the filamentary geometry observed, and hence the source volumes may have been overestimated;

(ii) Onishi et al. (2002) assumed a constant density value for each core. However, virial models involving this assumption are likely to lead to overestimates of mass in the cases where the actual density decreases outwards (MacLaren, Richardson & Wolfendale 1988).

While the $H^{13}CO^+$ peaks do not correlate well with the dust continuum, the situation is different for N_2H^+. This behaviour can be seen from Table 4 which includes the positional offsets between N_2H^+ and dust continuum peaks; the median offset is only 21 arcsec, i.e. only a third of the corresponding value for $H^{13}CO^+$ even though the resolution of the N_2H^+ observations (60 arcsec) was much coarser. Thus, the positional data provide no evidence for N_2H^+ freeze-out, and this is supported by the fact that the N_2H^+ detections seem preferentially associated with the coldest cores (the seven N_2H^+ detections include four of our five lowest temperature cores, all of which are cooler than 7 K). However, at higher resolution the situation may be different, since interferometric observations of ρ Oph have shown that the correspondence between dust emission and N_2H^+ clumps does indeed break down on spatial scales $\lesssim 10$ arcsec (Friesen et al. 2010). Theoretical models have, in fact, shown that within ~ 1000 au of the core centre, complete freeze-out of heavy elements is likely (Caselli 2011). Core profiling based on dust emission thus promises to make an important contribution to investigations of core chemistry by providing an independent method for estimating temperatures in the centres of cores.

Finally, our core no. 16 has been observed previously in the 850 μm continuum by Sadavoy et al. (2010) and given the designation JCMTSF_041950.8+271130. While the quoted 850 μm source radius of 0.019 pc is close to the COREFIT r_0 value of 0.015 ± 0.002 pc, the estimated masses are significantly different. The estimate of Sadavoy et al. (2010) is based on the observed 850 μm flux density and an assumed dust temperature of 13 K; this yielded $0.22 \, M_\odot$ which is a factor of ~ 5 smaller than our COREFIT value and most likely an underestimate resulting from too high an assumed temperature. This illustrates the large errors in mass which can occur in the absence of temperature information, as has been noted by others (Stamatellos et al. 2007; Hill et al. 2009, 2010).

8 CONCLUSIONS

The principal conclusions from this study can be summarized as follows.

(i) For this sample of cores, the dust temperatures estimated from SED fits, using spatially integrated fluxes and an isothermal model, are consistent with the spatially averaged temperatures derived from the COREFIT profiles. However, the masses obtained from the SED fits are systematically lower (by a factor of ~ 1.5) than those obtained

from detailed core profiling. The present statistical sample, however, is insufficient to obtain a definitive correction factor, the latter of which is likely to be dependent on mass and possibly environment (ISRF) also.

(ii) Estimates of central dust temperature are in the range 6–12 K. These temperatures are negatively correlated with peak column density, consistent with behaviour expected due to shielding of the core centre from the ISRF, assuming that the latter provides the sole heating mechanism. The model core temperatures obtained from radiative transfer calculations are, however, systematically ~ 2 K lower than the COREFIT estimates; it is not yet clear whether that difference has an astrophysical origin or is due to errors in model assumptions.

(iii) The radial falloff in density is, in the majority of cases, consistent with the $\alpha \simeq 2$ variation expected for Bonnor–Ebert spheres although exceptions are found in two cases, both of which appear to have steeper density profiles. Since both involve cores which are gravitationally unstable based on Bonnor–Ebert criteria, such behaviour may have implications for models of the early collapse phase.

(iv) The reliability of core stability estimates derived from isothermal models is not seriously impacted by the temperature gradients known to be present in cores. Thus, the preliminary classification of cores as gravitationally bound or unbound can be based on relatively simple criteria, facilitating statistical studies of large samples.

(v) Core locations do not correspond well with previously published locations of $H^{13}CO^+$ peaks, presumably because carbon-bearing molecules are frozen out in the central regions of the cores, most of which have dust temperatures below 10 K. The results suggest that the $H^{13}CO^+$ emission arises from dense gas in the filamentary region on either side of the core itself, in a dumbbell-like geometry, and that the radius of the sublimation zone is typically $\sim 10^4$ au.

(vi) The coldest cores are mostly detected in N_2H^+, and the N_2H^+ core locations are consistent with those inferred from dust emission, albeit at the relatively coarse (1 arcmin) resolution of the N_2H^+ data. Our data therefore do not show evidence of N_2H^+ freeze-out.

REFERENCES

André P., Ward-Thompson D., Motte F., 1996, A&A, 314, 625

André P. et al., 2010, A&A, 518, L102

Caselli P., 2011, in Cernicharo J., Bachiller R., eds, Proc. IAU Symp. 280, The Molecular Universe. Cambridge Univ. Press, Cambridge, p. 19

Elias J. H., 1978, ApJ, 224, 857

Evans N. J., II, Rawlings J. M. C., Shirley Y. L., Mundy L. G., 2001, ApJ, 557, 193

Friesen R. K., Di Francesco J., Shimajiri Y., Takakuwa S., 2010, ApJ, 708, 1002

Giannini T. et al., 2012, A&A, 539, A156

Griffin M. J. et al., 2010, A&A, 518, L3

Griffin M. J. et al., 2013, MNRAS, 434, 992

Hacar A., Tafalla M., Kauffmann J., Kovács A., 2013, A&A, 554, 55

Hildebrand R. H., 1983, QJRAS, 24, 267

Hill T., Pinte C., Minier V., Burton M. G., Cunningham M. R., 2009, MNRAS, 392, 768

Hill T., Longmore S. N., Pinte C., Cunningham M. R., Burton M. G., Minier V., 2010, MNRAS, 402, 2682

Kirk J. M. et al., 2013, MNRAS, 432, 1424

Könyves V. et al., 2010, A&A, 518, L106

Kramer C., Winnewisser G., 1991, A&AS, 89, 42

Lada C. J., Muench A. A., Rathborne J., Alves J. F., Lombardi M., 2008, ApJ, 672, 410

Li A., Draine B. T., 2001, ApJ, 554, 778

Lutz D., 2012, Herschel Document PICC-ME-TN-033, available at: http://herschel.esac.esa.int/twiki/pub/Public/PacsCalibrationWeb/bolopsf_20.pdf

MacLaren I., Richardson K. M., Wolfendale A. W., 1988, ApJ, 333, 821

Men'shchikov A., André Ph., Didelon P., Motte F., Hennemann M., Schneider N., 2012, A&A, 542, 81

Motte F., André Neri R., 1998, A&A, 336, 150

Motte F. et al., 2010, A&A, 518, L77

Onishi T., Mizuno A., Kawamura A., Tachihara K., Fukui Y., 2002, ApJ, 575, 950

Ott S., 2010, in Mizumoto Y., Morita K.-I., Ohishi M., eds, ASP Conf. Ser. Vol. 434, Astronomical Data Analysis Software and Systems XIX. Astron. Soc. Pac., San Francisco, p. 139

Palmeirim P. et al., 2013, A&A, 550, A38

Pilbratt G. L. et al., 2010, A&A, 518, L1

Plummer H. C., 1911, MNRAS, 71, 460

Poglitsch A. et al., 2010, A&A, 518, L2

Rousel H., 2013, PASP, 125, 1126

Roy A. et al., 2013, A&A, preprint (arXiv:1311.5086)

Sadavoy S. I. et al., 2010, ApJ, 710, 1247

Sipilä O., Harju J., Juvela M., 2011, A&A, 535, 49

Stamatellos D., Whitworth A. P., 2003, A&A, 407, 941

Stamatellos D., Whitworth A. P., Ward-Thompson D., 2007, MNRAS, 379, 1390

Tafalla M., Myers P. C., Caselli P., Walmsley C. M., 2004, A&A, 416, 191

Umemoto T., Kamazaki T., Sunada K., Kitamura Y., Hasegawa T., 2002, in Ikeuchi S., Hearnshaw J., Hanawa T., eds, Proc. IAU 8th Asian-Pacific Regional Meeting, Vol. II, Fragmentation in the ρ Ophiuchi Cluster Forming Region. Astron. Soc. Japan, Tokyo, p. 229

Vorobyov E. I., Basu S., 2005, MNRAS, 360, 675

Walmsley C. M., Flower D. R., Pineau Des Forêts G., 2004, in Pfalzner S., Kramer C., Staubmeier C., Heithausen A., eds, Proc. 4th Cologne-Bonn-Zermatt Symposium, Springer Proceedings in Physics, Vol. 91, The Dense Interstellar Medium in Galaxies. Springer, Berlin, p. 467

Ward-Thompson D., Scott P. F., Hills R. E., André P., 1994, MNRAS, 268, 276

Whalen A. D., 1971, Detection of Signals in Noise. Academic Press, New York

This paper has been typeset from a TEX/LATEX file prepared by the author.